Distance-dependent magnetization modulation induced by inter-superatomic interactions in Cr-doped $Au_6Te_{12}Se_8$ dimers

Yurou Guan(官雨柔)[1,2], Nanshu Liu(刘南舒)[1,2], Cong Wang(王聪)[1,2],
Fei Pang(庞斐)[1,2], Zhihai Cheng(程志海)[1,2], and Wei Ji(季威)[1,2,†]

[1] *Beijing Key Laboratory of Optoelectronic Functional Materials & Micro-Nano Devices, School of Physics,
Renmin University of China, Beijing 100872, China*

[2] *Key Laboratory of Quantum State Construction and Manipulation (Ministry of Education), Renmin University of China, Beijing 100872, China*

Individual superatoms are assembled into more complicated nanostructures to diversify their physical properties. Magnetism of assembled superatoms remains, however, ambiguous, particularly in terms of its distance dependence. Here, we report density functional theory calculations on the distance-dependent magnetism of transition metal embedded $Au_6Te_8Se_{12}$ (ATS) superatomic dimers. Among the four considered transition metals, which include V, Cr, Mn and Fe, the Cr-embedded $Au_6Te_{12}Se_8$ (Cr@ATS) is identified as the most suitable for exploring the inter-superatomic distance-dependent magnetism. We thus focused on Cr@ATS superatomic dimers and found an inter-superatomic magnetization-distance oscillation where three transitions occur for magnetic ordering and/or anisotropy at different inter-superatomic distances. As the inter-superatomic distance elongates, a ferromagnetism (FM)-to-antiferromagnetic (AFM) transition and a sequential AFM-to-FM transition occur, ascribed to competitions among Pauli repulsion and kinetic-energy-gains in formed inter-superatomic Cr–Au–Au–Cr covalent bonds and Te–Te quasi-covalent bonds. For the third transition, in-plane electronic hybridization contributes to the stabilization of the AFM configuration. This work unveils two mechanisms for tuning magnetism through non-covalent interactions and provides a strategy for manipulating magnetism in superatomic assemblies.

1. Introduction

Superatoms,[1,2] also known as clusters, as a kind of candidate for the third dimension of the periodic table of cluster elements,[3] have attracted increasing attention in the past few decades.[3–8] Like atoms, superatoms could be potentially assembled into larger-scale structures in a controllable manner, ascribed to their considerable individual stability and directional inter-superatomic interactions.[9–11] Among them, magnetic superatoms[12] are of particular interest. They could be used to construct magnetic superatomic materials with tunable inter-superatomic distances,[13] coordination numbers,[14] and thus magnetism.[15,16] The magnetism was intensively studied for individual superatoms, like Cr@Si$_{12}$,[15,16] Ti@Au$_{14}$,[15] and U@B$_{40}$[15] which could be theoretically assembled into dimers through covalent bonding. Density functional theory (DFT) calculations also predicted, e.g., a free-electron-mediated ferromagnetic (FM) V@Si$_{12}$ sheet,[14] antiferromagnetic (AFM) Cs$_2$[Ti@Ge$_{16}$], Cs$_2$[W@Si$_{12}$] superatomic monolayers,[15] FM/ferrimagnetic (FiM)/AFM fullerene-based U$_2$C@C$_{80}$-M (M = Cr, Mn, Mo, and Ru) one-dimensional chains,[17] and an one-dimensional AFM chain comprised of AgCu nanoclusters bonded through sulfur atoms. The last was successfully realized in experiments, in which the coupling mechanism was assessed

to the antiferromagnetic super-exchange mediated by S 3p orbital.[13] It was well known that magnetic interactions highly depend on the distance and wavefunction overlapping among magnetic sites.[18–23] However, modulation of covalently bonded superatoms is energetically costly and often weakens the stability of the superatoms. An interesting question thus arises whether there is a category magnetic superatomic structures exhibiting feasibly controlled inter-superatomic distances and preserved thermal stability.

Unlike covalent bonding, non-covalent inter-superatomic interactions have an order of magnitude smaller scale, i.e., ~ 0.1 eV, for cohesive energies, which offer a much more feasible route to finely tune inter-superatomic positions. A ligand-free superatomic crystal, composed of $Au_6Te_{12}Se_8$ (ATS) cubic clusters solely, was experimentally synthesized in 2017[24] and was found in a natural mineral in 2020,[25] which seems an ideal parent compound for building magnetic superatomic materials. In the past few years, geometric and electronic structures, novel electronic states[26] and inter-superatomic interactions[24,27,28] of the ATS crystal were studied both experimentally and theoretically. In an ATS monomer, Au–Te and Se–Te sigma bonds stabilize the cluster skeleton and six frontier orbitals comprised of Te 5p orbitals govern the inter-superatomic non-covalent interactions.[26] Sim-

ilar non-covalent interactions, known as "covalent-like quasi-bonding" (CLQB),[29] were extensively investigated for inter-layer interactions of two-dimensional materials exhibiting distinct layer-dependent electronic,[29] optical,[30] thermal,[29,31] vibrational[32–34] and magnetic[18,19,35] properties. The ATS superatom is a cubically caged cluster, each of which could embed a single magnetic, usually transition metal (TM) atom, introducing a local magnetic moment. Although these metal-embedded clusters have yet to be synthesized experimentally, assemblies of such TM@ATS superatoms could, most likely, provide a magnetic platform allowing feasible and finely tuning of magnetic properties, in which the tuning mechanisms are largely unidentified so far.

In this work, we theoretically considered four 3d TM metal embedded ATS superatoms, namely, V, Cr, Mn, and Fe, using density functional theory calculations. Among them, the Cr@ATS superatom exhibited an inter-superatomic-distance-dependent magnetic oscillation behavior in its dimers. This oscillation was reflected in three AFM–FM transitions, the mechanisms of which were uncovered by examining their spin-polarized differential charge density and partial charge density of certain states, and by summarizing models for spin-exchange interactions and electronic hybridization of spin-polarized frontier orbitals. In addition, we also inspected the distance-dependent magnetic anisotropy of the dimer where, at least, contains two transitions between in- and out-planes.

2. Computational methods

Our density functional theory (DFT) calculations were carried out using the generalized gradient approximation and the projector augmented wave method[36,37] as implemented in the Vienna *ab-initio* simulation package (VASP).[38] Only the Gamma point was used to sample the Brillouin zone for all superatom monomer and dimer calculations. A kinetic energy cutoff of 500 eV for the plane-wave basis set was used for structural relaxations and total energy calculations, which ensures the convergence of the relative energies better than 1 meV/Cr@ATS. A sufficiently large vacuum layer of over 15 Å was adopted to eliminate imaging interactions with adjacent periods. To utilize controlled change of the inter-superatomic distance, we constrained the z coordinates of those eight outermost Se atoms of the Cr@ATS dimers (black dash circles in Fig. 2(a) and Figs. S1–S2). The rest atoms were allowed to relax until the residual force per atom was less than 0.01 eV/Å in all structural relaxations. Dispersion correction was made at the zero-damped PBE-D3 level,[39] which was proved to be accurate in describing structural-related properties[40] and was adopted in many previous calculations.[15,40,41] To calculate the magnetic anisotropy energy (MAE), we considered a series of orientations for the magnetic moment (see Fig. 6(a)), calculated the total energy for each orientation, and compared these energies to determine the easy-axis and the MAE value. These energies are relative ones so that they show good kinetic energy convergence. Thus, a cutoff of 500 eV for the kinetic energy and using the Gamma point for sampling the BZ are sufficient to derive these "tiny" energies. The kinetic energy cutoff used in this work is comparable to those used in e.g. Refs. [19,35,42,43].

We also considered the effects from the variation of the on-site Coulomb U values (ranging from 1 eV to 4 eV) on the TM@ATS superatoms, as presented in Fig. S3. The U value to represent the on-site Coulomb interactions on the Cr 3d orbitals of Cr@ATS was consistent with those tested and adopted in the CrI$_3$ bilayer, namely, U_{eff} value of 2.8 eV (with $U = 3.9$ eV and $J = 1.1$ eV).[18] Consequently, U values of 2.0 eV, 3.0 eV, and 4.0 eV were considered in the V, Mn, and Fe-doped ATS monomers, respectively.

3. Results and discussion

The ATS cluster has a sufficiently large atomic cage, with an face-to-face Au–Au distance of 5.7 Å, to embed individual transition metal atoms (see Fig. S4 for geometric and electronic structural details). We considered four transition metals, namely, V, Cr, Mn, and Fe, for embedding, the embedded ATS superatom of each of which is dynamically stable that no imaginary frequency was found in their vibrational spectra (see Fig. S5). This embedment also keeps the original O_h symmetry of ATS unchanged in TM@ATS superatoms (Fig. 1(a) & Tabel S1). While each of these four embedded superatoms could be feasibly synthesized in reasonably wide ranges of chemical potentials. Given the strong TM–Au–Au–TM covalent bonding in dimer resulting from the open-shell structure of Mn@ATS and V@ATS, and the excessive sensitivity of the magnetic ground state of Fe@ATS assemblies to their local geometric structure (see Fig. S6 for details), we chose to investigate Cr@ATS due to its superior stability and controllability in the distance-dependent magnetic behavior between superatoms. Therefore, the following discussion will focus on the Cr@ATS superatom.

Each Cr@ATS superatom contains six valence electrons originating from the embedding Cr atom (yellow arrows in Fig. 1(b)). Two of them hybridize with two Au 5p$_z$ electrons, forming two Cr–Au σ bonding states sitting at 7.05 eV (4.63 eV) below the vacuum level (Fermi level, red dashed line in Fig. 1(b)). A full energy diagram was plotted and discussed in Fig. S7. Each of these two bonding states resides around Cr–Au bonds oriented in all the x, y, and z directions (Fig. 1(c)). Among the remaining four electrons, three of them fully fill three Cr 3d t$_{2g}$ spin-up orbitals (gray levels in Fig. 1(b)) and the rest one fills the spin-up component of one e$_g$ orbital (blue levels in Fig. 1(b)). The intrinsic spin-up

HOMO state of ATS becomes empty and back donate an electron (up green arrow in Fig. 1(b)) to a spin-up Cr 3d e_g orbital, causing the five Cr 3d orbitals to be half-occupied and a large local magnetic moment of 4.15 μ_B. This occupation configuration explains the maintained O_h symmetry of Cr@ATS. The remaining one electron from the pristine HOMO and two electrons originating from deeper level(s) of pristine ATS are filled into the spin-down HOMO and one LUMO (double degener-ate) states of the pristine ATS. These three spin-down electrons provide anti-parallel spins (Fig. 1(d)) to screen the large magnetic moment of the Cr atom, resulting in a total net magnetic moment of 2.0 μ_B for Cr@ATS. After Cr embedding, the original real space distribution and degeneracy of six frontier orbitals of pristine ATS nearly maintain, as detailly compared in Fig. S8, indicating comparable non-covalent interactions in assemblies comprised of ATS or Cr@ATS.
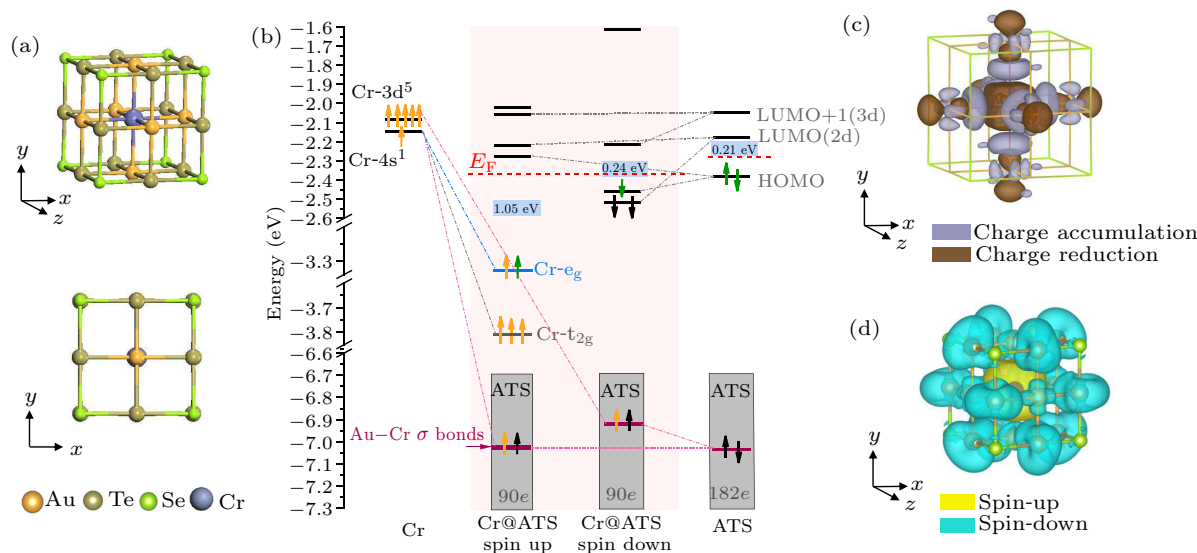

Fig. 1. Structure and properties of the Cr@ATS superatomic monomer. (a) Perspective (up) and top (down) views for the atomic structure of the Cr@ATS superatom. (b) Energy level alignments for the Cr atom, the spin-polarized Cr@ATS monomer, and the pristine ATS cage. All energies are aligned to the vacuum level, and the Fermi level is denoted by the red dashed line. Those gray boxes represent deeper levels not shown in the diagram and the total numbers of electrons filling these levels are listed at the bottom of each box. (c) Differential charge density between the Cr atom and the ATS cage. Purple and brown density contours represent charge accumulation and charge reduction, respectively, with an isosurface value of 0.004 e/Bohr^3. (d) Spin density of the Cr@ATS monomer while yellow (blue) contours correspond to spin-up (-down) electron densities. An isosurface value of 0.0003 e/Bohr^3 was used.

To simplify our discussion, we focused on the simplest Cr@ATS assembly, namely, a Cr@ATS dimer (Fig. 2(a)), for modeling the distance evolution of magnetism. A face-to-face, without sliding in the x–y plane, stacking configuration (Fig. 2(b)) is, at least, 0.42 eV lower in energy than other dimer configurations, (see Fig. S9 for more details). At the equilibrium distance $d_E = 3.32$ Å, we calculated the vibrational frequencies of a fully relaxed Cr@ATS dimer. No appreciable imaginary frequencies were found in the vibrational spectrum, with the wave number for the lowest energy non-zero mode being 12.12 cm^{-1}, verifying the dynamic stability of ATS and the non-covalent inter-superatomic interaction in the ATS dimer.

The Cr@ATS dimer favors inter-superatomic ferromagnetic (FM) coupling through inter-superatomic non-covalent interactions, i.e., covalent-like quasi-bonding.[44] The inter-superatomic interactions also break down the cubic symmetry of the Cr@ATS monomer that each Cr atom moves 0.09 Å towards each other. In the meantime, the interfacial faces of the two superatoms expand where the side length enlarges from 5.50 Å to 5.64 Å (Fig. 2(b)). Such structural distortion leads to an electrical polarization in individual ATS superatoms, form-ing an anti-parallel polarization in the ATS dimer (red arrows in Fig. 2(a)). The structural distortion, consequently, lifts the original degeneracy of the e_g orbitals that the energy of the Cr $d_{x^2-y^2}$ orbital becomes higher than that of the Cr d_{z^2} orbital (see Fig. S10).

Magnetism of a series of dimer structures with different inter-superatomic Au–Au distances (d_{Au-Au}, Fig. 2(a)) was considered. The z-coordinates of the eight outermost Se atoms (marked by black dash circles in Figs. 2(a) and 2(b)) were kept fixed to maintain certain inter-superatomic distances off the equilibrium as we mentioned in the Section 2. Figure 3(c) plots the energy difference between the inter-superatomic AFM and FM configurations as a function of d_{Au-Au}, in which the initial structures for relaxation were constructed by stretching the inter-superatomic distance from the equilibrium step by step. Interestingly, a magnetic oscillation behavior is found as the Au–Au distance increases, unlike the Bethe–Slater curve-like behavior observed in magnetic bilayers,[35] although their interfacial interactions are all governed by non-covalent interactions. While there are three transitions (T$_1$ to T$_3$) of the magnetic ground state of the

ATS dimer, the first one (T_1) occurs at $d_{T1} = 3.77$ Å where the dimer becomes to favor the AFM coupling from the FM one. The AFM coupling persists to $d_{T2} = 4.21$ Å, at which the second transition emerges that the dimer prefers the FM coupling again, but with slightly smaller magnetization values (Fig. 2(d)) and FM–AFM energy differences than those at distances below d_{T1}. The second FM to AFM transition happens at $d_{T3} = 4.80$ Å that the AFM coupling favors again. Eventually, the energies of AFM and FM tend to degenerate when $d > 5.9$ Å. Consideration of SOC does not significantly change these results. Similar distance-dependent magnetic oscillation behavior is also observed in one-dimensional Cr@ATS chains, as discussed in Fig. S11. The magnetization–distance oscillation behavior found in the dimer also indicates a piezomagnetic effect showing out-of-plane piezomagnetic coefficient d_{33} in alternating signs. The d_{33} reaches -5.1 emu/g/kbar at transition T1 where the magnetization eliminates from over 8.7 μ_B within a distance change of 0.12 Å. A positive $d_{33} = 2.9$ emu/g/kbar is obtained at transition T2 where the magnetization increases from 0.0 μ_B to 6.3 μ_B within 0.20 Å. These predicted piezomagnetic coefficients under zero magnetic field exhibit comparable performance to those of conventional bulk piezomagnetic materials like MnGaN (1.9 emu/g/kbar)[45] and MnNiGe (5.3 emu/g/kbar)[46] measured at low temperatures and under strong magnetic fields.
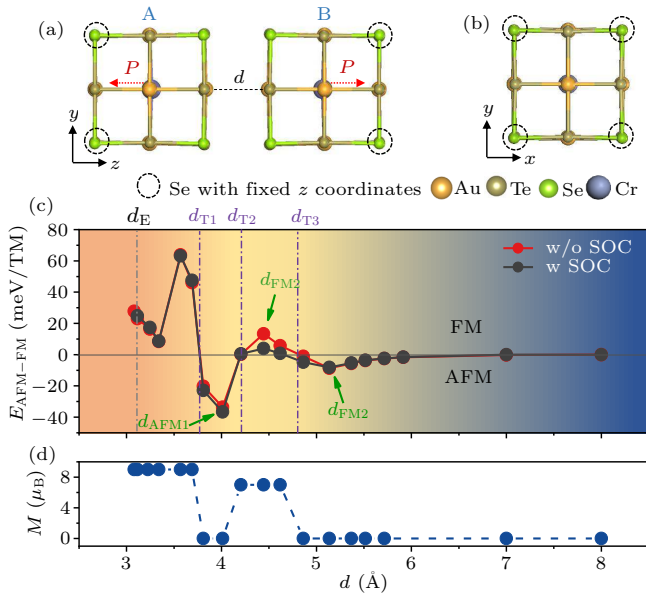

Fig. 2. Magnetization–distance oscillation in Cr@ATS superatomic dimers. Top (a) and side (b) views of the atomic structure for the Cr@ATS dimer. The red arrows mark the polarization directions. The inter-superatom distance d_{Au-Au} is defined as the interfacial Au–Au distance. (c) Total-energy differences between the inter-superatom AFM/FM configurations as a function of inter-superatom distances d_{Au-Au}. Black (red) dots denote the data calculated with (without) consideration of spin–orbit coupling. In this series of data, structural relaxations were done by stretching the inter-superatomic distance from the equilibrium step by step. The equilibrium and three transition distances are denoted using gray and purple dot-dashed lines and the three green arrows indicate three representative distances for phases AFM1, FM2, and AFM2. (d) Evolution of the corresponding total magnetic moment on the Cr@ATS dimer as a function of inter-superatomic distance d_{Au-Au}.

These three transitions provide more fruitful phenomena than the previously found BSC-like behavior[35] for understanding spin-exchange mechanism through non-covalent interfaces. We thus selected four characteristic d_{Au-Au} values, namely, the equilibrium distance $d_E = 3.32$ Å, and the most representative distance of each FM or AFM region at $d_{AFM1} = 4.01$ Å, $d_{FM2} = 4.52$ Å and $d_{AFM2} = 5.11$ Å, which cover all three transitions. At $d_E = 3.32$ Å, the interfacial charge density strongly redistributes upon formation of the dimer, as shown in Figs. 3(a) and 3(b) for the spin-up (-down) component, which indicates interfacial Te–Te and Cr–Au–Au–Cr interactions. Those states, primarily contributed from the interfacial Se atoms, however, reside at least 1.24 eV below E_F, playing a minor role for the interfacial interactions, as more comprehensively discussed in Fig. S12.

Significant wavefunction overlaps are obtained for both spin components between interfacial Te 5p orbitals, which is known as the previously found Te–Te CLQB[35] (highlighted by blue dashed boxes in Fig. 3(a)). Additionally, electrons of the two Cr atoms directly interact through the spin-up component of the electronically hybridized Cr $3d_{z^2}$ and Au $5d_{z^2}$ bonding state (Figs. 3(a) and 3(c)), forming a Cr–Au–Au–Cr bonding state (highlighted in the red dashed box of Fig. 3(c)). This bonding state is the spin-up HOMO state for the formed dimer, while the spin-down component is not involved in forming it (Fig. 3(d)). Such electronic hybridization among Cr_A, Cr_B, and interfacial Au atoms delocalizes spin-up electrons of the d_{z^2} orbital of each Cr site (Cr_A or Cr_B) [denoted by red dashed circle in Fig. 3(e)]. Thus, the delocalization yields substantial kinetic energy gains that are strong enough to suppress the Pauli repulsion between interfacial Te p_z orbitals in the Te CLQBs, thus resulting in the FM coupling between the two ATS superatoms in the dimer. If the dimer took the AFM coupling in favor of the Pauli repulsion, the Cr–Au–Au–Cr bonding would not be able to form between different spin components. Consequently, the direct spin-exchange coupling breakdowns for the spin-up component among the Cr and Au sites (Figs. 4(f), see Fig. S12 for more details). In other words, the direct Cr–Au–Au–Cr spin-exchange between Cr@ATS superatoms maintains the superior stability of the inter-superatomic FM configuration for Cr@ATS dimer at the shorter range of inter-superatomic distances.

At $d_{AFM1} = 4.01$ Å, a longer distance, the Cr–Au–Au–Cr hybridization eliminates just before $d_{T1} = 3.77$ Å ($d = 3.69$ Å), leaving the Te–Te interaction solely at the inter-superatomic interface (Figs. 3(g) and 3(h), see Fig. S13 for more details). Thus, the change of the inter-superatomic magnetism as a function of distance follows the BSC-like behavior previously found in magnetic bilayers,[35] namely, a distance-induced AFM–FM transition ascribed to the competition between Pauli (Coulomb) repulsion and kinetic energy gain. It

is worth noting that the AFM-to-FM transition distance in the Cr@ATS dimer $d_{T2} = 4.21$ Å is highly comparable to the value (4.22 Å) previously predicted in the CrTe$_2$ bilayer. The details of the AFM-to-FM transition were intensively discussed in Ref. [35], we ensured the mechanism is shared between the Cr@ATS dimer and the CrTe$_2$ bilayer by examining plots of their ρ_{DCD} and $|\psi|^2$ at $d_{AFM1} = 4.01$ Å. Both the spin-up (Fig. 3(g)) and -down (Fig. 3(h)) components have accumulated electron densities at the overlapping region of the inter-superatom interface, leading to spin antiparallel polarized Te

5p$_z$ orbitals (illustrated in Fig. 3(k) and highlighted by the green ellipse). These density plots are analogical to those found in the CrTe$_2$ bilayer, indicating the mechanism explaining the BSC behavior governs at the inter-supertomic interface of the Cr@ATS dimer. Particularly, the Pauli repulsion dominates at shorter distances, giving rise to the AFM coupling. The repulsion weakens and the kinetic energy gain governs at slightly longer distances, preferring the FM coupling, as illustrated in Fig. 3(l).
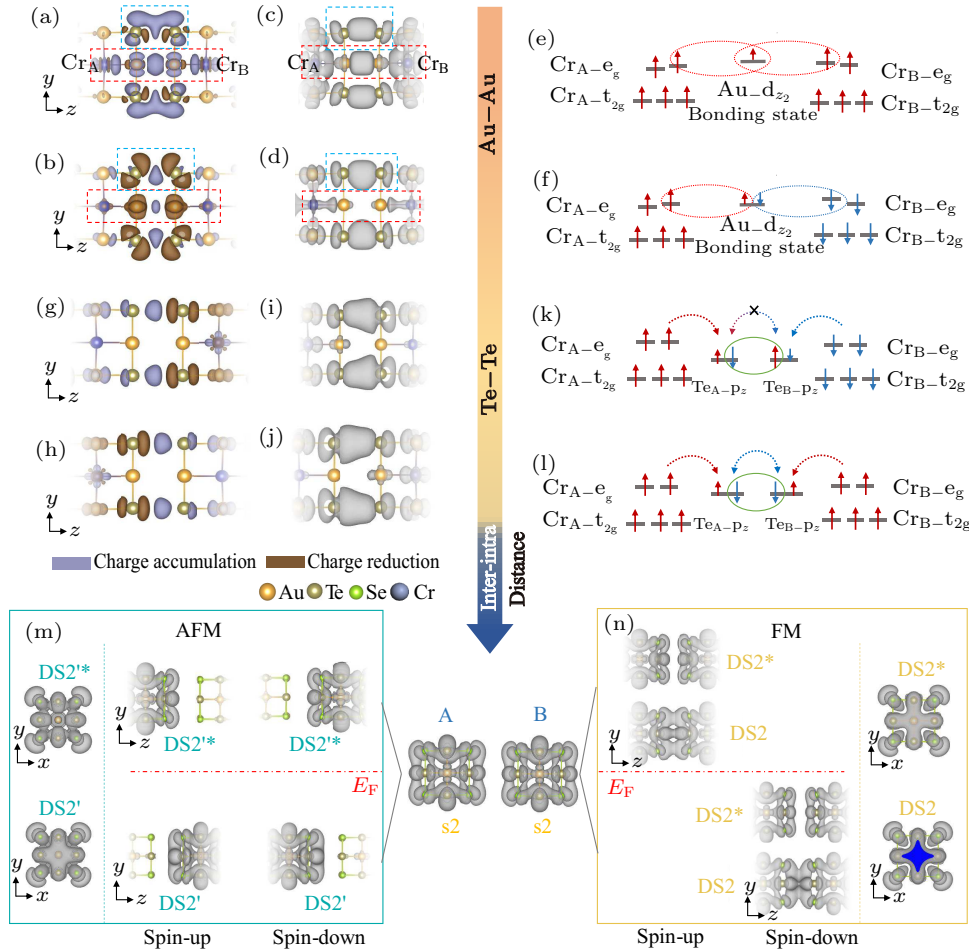

Fig. 3. Triple competing interactions and coupling mechanisms in Cr@ATS dimers. The colorized arrow indicates superatomic distance d increasing, in which three types of primary interactions are denoted in colors orange, yellow, and dark blue. Spin-up (a) and -down (b) components of the differential charge densities for the Cr@ATS dimer at equilibrium distance $d_E = 3.32$ Å. Purple and brown contours denote charge accumulation and reduction, and the isosurface value is set to 0.0005 e/Bohr^3. The spin-up (c) and -down (d) components of the partial density of states for the inter-superatomic bonding state are plotted. Those red dash frames highlight the Au–Au interaction and the bonding state and those blue dash frames indicate the Te–Te covalent-like quasi-bonding. (e) and (f) illustrate the FM and AFM exchanges dominated by the Au 5d$_{z^2}$ bonding state. Panels (g)–(j) replot those depicted in (a)–(d) for $d_{AFM1} = 4.01$ Å, namely, differential charge densities (g), (h) and partial charge densities (i), (j) for the spin-up (g), (i) and -down (h), (j) components. Panels (k) and (l) plot the diagrams for the AFM and FM spin-exchanges dominated by Te 5p$_z$ wave-function overlaps. Green circles denote the overlapping region. Spin-up and -down electrons are represented by red straight-up and blue straight-down arrows, the length of which qualitatively represents the number of spin-polarized electrons. To facilitate the discussion of exchange mechanisms, we denote the left and right superatoms as A and B, respectively. Panel m (n) plots the visualized wave-function norms of the AFM (FM) coupling in the Cr@ATS dimer at $d_{AFM2} = 5.11$ Å, with DSx and DSx^* indicating bonding and antibonding states of the dimer.

When the inter-superatomic distance further increases, an unusual FM–AFM transition (T$_3$) occurs at d_{T3} after the second FM state, ascribed to a characteristic hybridization between the in-plane orbitals of each Cr@ATS superatom. The FM and AFM configurations in the AFM2 region ($d > d_{T3}$, Figs. 3(m), 3(n), 4) differ by the distance dependence of the s2

frontier orbital (see Fig. S8 for more details) of each Cr@ATS superatom. Figure 4(a) clearly shows that the hybridization splitting of orbital s2 maintains at ~ 0.29 eV up to $d = 8.0$ Å in the inter-superatomic AFM configuration, while that in the FM configuration gradually decreases to zero as a function of d (Fig. 4(b)). Thus, the FM to AFM transition T$_3$ is, most likely,

directly relevant to the different s2 hybridizations in the FM and AFM configurations. In the AFM configuration, the s2 state is prone to hybridize in the x–y plane (Fig. 3(m)), forming an occupied bonding (DS2′) and an unoccupied antibonding state (DS2′*) for both the spin-up and -down components at the A and B Cr@ATS superatoms (see Fig. S14 for details).

However, in the FM configuration, the occupied states contain a pair of bonding and antibonding states for only the spin-down component (Fig. 3(n), see Fig. S14 for more details). Thus, the one more bonding state occupied in the AFM configuration further stabilizes the inter-superatomic AFM configuration, leading to the FM to AFM transition in region AFM2.
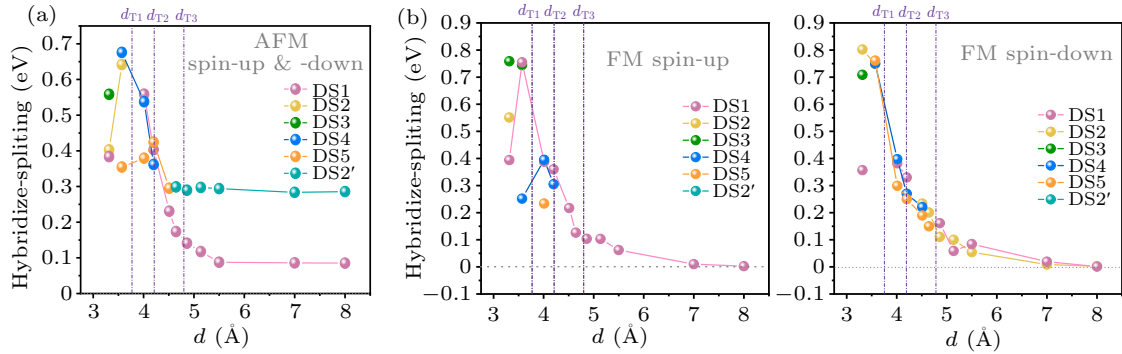

Fig. 4. Distance-dependent hybridization splitting energies. Summarized electronic hybridization splitting energies as a function of the inter-superatomic distance for those six frontier orbitals of the Cr@ATS dimer (DS1 to DS5 and DS2′) in the inter-superatomic AFM (a) and FM (b) configurations.

In short, three competing mechanisms lead to the distance-dependent magnetic oscillation behavior in the Cr@ATS dimer. At a shorter inter-superatomic distance, a direct exchange is determined by the Au–Au binding state, leading to an FM ground state (orange part of the colorized arrow shown in the middle of Fig. 3). At slightly larger distances, the distance-dependent Te–Te interaction,[35] together with the gradually eliminated Au–Au interaction, results in the FM-to-AFM and the subsequent BSC-like AFM-to-FM transitions, as

shown in the yellow part of the colorized arrow in Fig. 3. As the distance further enlarges, the in-plane electronic hybridization of frontier orbitals, rather than out-of-plane interfacial ones, drives the second FM-to-AFM transition (dark blue part of the colorized arrow in Fig. 3). Furthermore, this distance-dependent magnetic oscillation behavior does not follow the Ruderman–Kittel–Kasuya–Yosida (RKKY)[47–50] interactions because of insufficient density of states near the Fermi level to support the itinerant electron hoping mechanism.
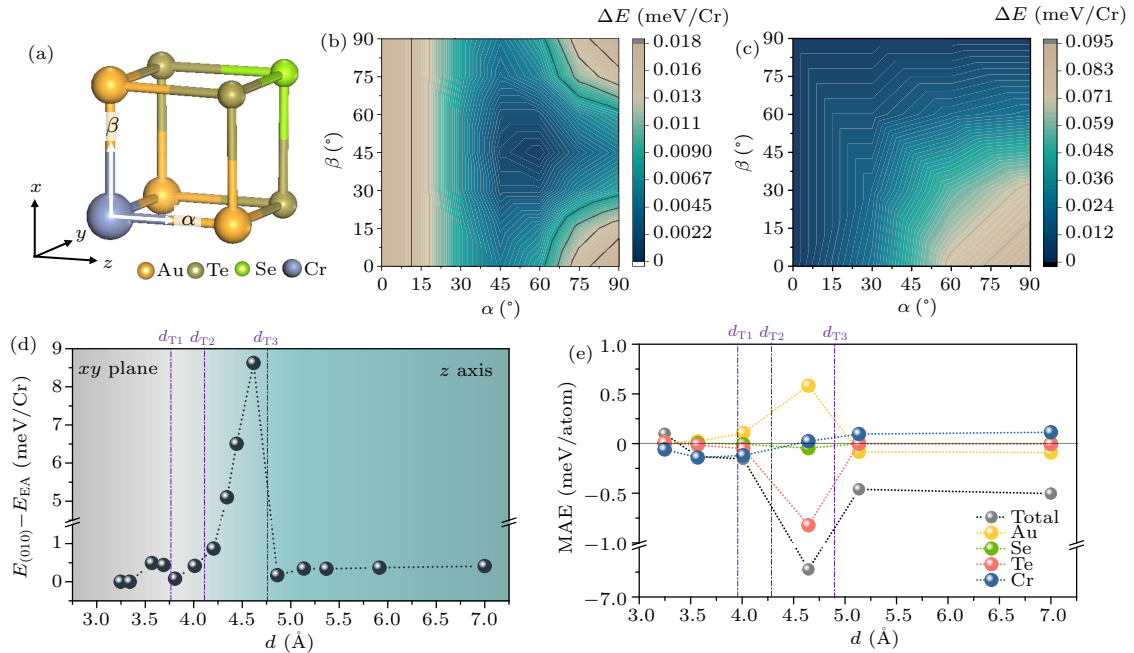

Fig. 5. Magnetic anisotropy energy and magnetic easy axis. (a) Axis to define the direction of the easy magnetization. Angle α (β) corresponds to the angles between the magnetization direction and the z (x) axis. Angular dependences of the MAE for the Cr@ATS monomer (b) and dimer at $d_E = 3.32$ Å (c). A step size of 15° was used in the calculations. The zero-energy reference was chosen to be the total energy of the monomer or dimer where the magnetic moment on Cr points to the z-axis. (d) Energy difference $E_{(010)} - E_{(EA)}$ as a function of inter-superatomic Au–Au distance d. Three transition distances are marked for reference and the gray and green background colors indicate the regions where the magnetization direction is oriented in the xy plane or along the z axis. (e) Torque analysis for elemental decomposed MAE contributions.

We defined the orientations and angles for examining the magnetic anisotropy energies (MAEs) of the Cr@ATS monolayer in Fig. 5(a). The easy magnetization axis of the Cr@ATS monomer orients in the direction of $\alpha = 60°$ and $\beta = 45°$. The energy difference between easy and hard axes is 0.02 meV/Cr (Fig. 5(b)), which increases to 0.09 meV/Cr in the Cr@ATS dimer at the equilibrium distance $d_E = 3.32$ Å (Fig. 5(c)), accompanied by the magnetization reorients towards the x–y plane. Figure 5(d) plots the MAE–distance relations of the Cr@ATS dimer, where the $E_{(010)} - E_{(EA)}$ value gradually increases up to over 8 meV/Cr before an abrupt drop to nearly zero. The maximum value of 8.62 meV/Cr is found at $d = 4.52$ Å where the dimer is in the FM configuration. In addition, as the distance increases, the easy magnetization axis rotates from the xy-plane to the z-axis. These magnetic anisotropy changes are examined by plotting the distance-dependent elemental contribution to MAE in Fig. 5(e), in which positive (negative) values indicate the easy magnetization axis favoring the out-of-plane (in-plane) direction. The plot clearly indicates that the contribution of Te atoms is the strongest in the region with significantly enhanced MAE, which corresponds to the FM magnetic state dominated by Te–Te CLQBs.

4. Conclusions

In summary, we theoretically predicted magnetization-distance oscillation and in- to out-of-plane magnetic anisotropy transition behaviors in the Cr embedded ATS superatomic dimer. From the oscillation behavior, we uncovered two mechanisms in addition to previously known magnetic transition mechanisms at non-covalently bonded interfaces. The Cr@ATS superatom is the most suitable for investigating the inter-superatomic distance-dependent magnetism among four ATS superatoms embedded by transition metals V, Mn, Fe and Cr. The predicted inter-superatomic magnetization varies alternately between FM and AFM as a function of inter-superatomic distance d, accompanied by three magnetic transitions (T1 to T3) at $d_{T1} = 3.77$ Å (FM-to-AFM), $d_{T2} = 4.21$ Å (AFM-to-FM), and $d_{T3} = 4.80$ Å (FM-to-AFM). One of the two additional mechanisms lies in the competition of electron delocalization through the inter-superatomic Cr–Au–Au–Cr hybridization and the Pauli (Coulomb) repulsion between electrons of inter-superatomic Te atoms, which leads to transition T1. The equilibrium inter-superatomic distance (3.32 Å) and the transition distance (4.21 Å) for T2 (AFM-to-FM) are highly comparable to those of bilayer CrTe$_2$, indicating transition T2 shares the same mechanism with the previously found Bethe–Slater-curve-like (AFM-to-FM) transition in bilayer CrTe$_2$.[35] Transition T3 is, however, caused by an in-plane electronic hybridization although the transition occurs in the out-of-plane (inter-superatomic) direction, which is unique and is expected to be general for superatoms.

This distance-dependent magnetic oscillation behavior indicates the application potential of Cr@ATS superatoms in spintronic, piezomagnetic and other mechanical-magnetic devices minimized down to the atomic limit. Besides the Cr@ATS dimers we studied in this work, TM@ATS or other caged superatoms are expected to form more complex assembly structures, e.g., chains, ribbons, or layers. These assemblies could offer more fruitful results on inter-superatomic electronic interactions that substantially tune their electrical, optical, magnetic, mechanical, and even catalytic properties. We infer that these results could shed considerable light on developing a universal and feasible route to tailor superatomic materials.

References

[1] Khanna S N and Jena P 1992 *Phys. Rev. Lett.* **69** 1664
[2] Khanna S N and Jena P 1995 *Phys. Rev. B* **51** 13705
[3] Luo Z and Castleman A W 2014 *Acc. Chem. Res.* **47** 2931
[4] Reber A C and Khanna S A O 2017 *Acc. Chem. Res.* **50** 255
[5] Jena P and Sun Q 2018 *Chemical Reviews* **118** 5755
[6] Doud E A, Voevodin A, Hochuli T J, Champsaur A M, Nuckolls C and Roy X 2020 *Nat. Rev. Mater.* **5** 371
[7] Gao Y and Wang Z 2016 *Chin. Phys. B* **25** 083102
[8] Feng M, Zhao J, Huang T, Zhu X and Petek H 2011 *Acc. Chem. Res.* **44** 360
[9] Yin B and Luo Z 2021 *Coord. Chem. Rev.* **429** 213643
[10] Claridge S A, Castleman A W, Jr., Khanna S N, Murray C B, Sen A and Weiss P S 2009 *ACS Nano* **3** 244
[11] Yu F, Liu Z, Li J, Huang W, Yang X and Wang Z 2022 *Chin. Phys. B* **31** 128107
[12] Zhao J, Huang X, Jin P and Chen Z 2015 *Coord. Chem. Rev.* **289–290** 315
[13] Xia N, Xing J, Peng D, Ji S, Zha J, Yan N, Su Y, Jiang X, Zeng Z, Zhao J and Wu Z 2022 *Nat. Commun.* **13** 5934
[14] Liu Z, Wang X Q, Cai J and Zhu H 2015 *J. Phys. Chem. C* **119** 1517
[15] Du Q, Wang Z, Zhou S, Zhao J and Kumar V 2021 *Phys. Rev. Mater.* **5** 066001
[16] Robles R and Khanna S N 2009 *Phys. Rev. B* **80** 115414
[17] Zhao Y, Guo Y, Qi Y, Jiang X, Su Y and Zhao J 2023 *Adv. Sci.* **10** 2301265
[18] Jiang P, Wang C, Chen D, Zhong Z, Yuan Z, Lu Z and Ji W 2019 *Phys. Rev. B* **99** 144401
[19] Wu L, Zhou L, Zhou X, Wang C and Ji W 2022 *Phys. Rev. B* **106** L081401
[20] Wang Y, Wang C, Liang S, Ma Z, Xu K, Liu X, Zhang L, Admasu A S, Cheong S W, Wang L, Chen M, Liu Z, Cheng B, Ji W and Miao F 2020 *Adv. Mater.* **32** 2004533
[21] Lv H Y, Lu W J, Shao D F, Liu Y and Sun Y P 2015 *Phys. Rev. B* **92** 214419

[22] Xian J, Wang C, Nie J, Li R, Han M, Lin J, Zhang W, Liu Z, Zhang Z, Miao M, Yi Y, Wu S, Chen X, Han J, Xia Z, Ji W and Fu Y 2022 *Nat. Commun.* **13** 257

[23] Li B, Wan Z, Wang C, Chen P, Huang B, Cheng X, Qian Q, Li J, Zhang Z, Sun G, Zhao B, Ma H, Wu R, Wei Z, Liu Y, Liao L, Ye Y, Huang Y, Xu X, Duan X, Ji W and Duan X 2021 *Nat. Mater.* **20** 818

[24] Guo J G, Chen X, Jia X Y, Zhang Q H, Liu N, Lei H C, Li S Y, Gu L, Jin S F and Chen X L 2017 *Nat. Commun.* **8** 871

[25] Bobrova O V, Kasatkin A V, Laufek F, Nestola F, Plášil J, Tolstykh N D, Tuhý M and Vymazalová A 2020 *Mineral. Mag.* **84** 117

[26] Xing S, Wu L, Wang Z, Chen X, Liu H, Han S, Lei L, Zhou L, Zheng Q, Huang L, Lin X, Chen S, Xie L, Chen X, Gao H, Cheng Z, Guo J, Wang S and Ji W 2022 *Phys. Rev. X* **12** 041034

[27] Chen X, Fei G, Song Y, Ying T, Huang D, Pan B, Yang D, Yang X, Chen K, Zhan X, Wang J, Zhang Q, Li Y, Gu L, Gou H, Chen X, Li S, Cheng J, Liu X, Hosono H, Guo J G and Chen X 2022 *J. Am. Chem. Soc.* **144** 20915

[28] Jia X, Yu Y, Chen X, Guo J, Ying T, He L, Chen X and Li S 2018 *Chin. Phys. B* **27** 067401

[29] Zhao Y, Qiao J, Yu P, Hu Z, Lin Z, Lau S P, Liu Z, Ji W and Chai Y 2016 *Adv. Mater.* **28** 2399

[30] Mak K F, Sfeir M Y, Wu Y, Lui C H, Misewich J A and Heinz T F 2008 *Phys. Rev. Lett.* **101** 196405

[31] Qiao J, Kong X, Hu Z-X, Yang F and Ji W 2014 *Nat. Commun.* **5** 4475

[32] Wu J B, Hu Z X, Zhang X, Han W P, Lu Y, Shi W, Qiao X F, Ijiäs M, Milana S, Ji W, Ferrari A C and Tan P H 2015 *ACS Nano* **9** 7440

[33] Puretzky A A, Oyedele A D, Xiao K, Haglund A V, Sumpter B G, Mandrus D, Geohegan D B and Liang L 2018 *2D Mater.* **5** 035016

[34] Hu Z, Kong X, Qiao J, Normand B and Ji W 2016 *Nanoscale* **8** 2740

[35] Wang C, Zhou X, Zhou L, Pan Y, Lu Z, Wan X, Wang X and Ji W 2020 *Phys. Rev. B* **102** 020402

[36] Blochl P E 1994 *Phys. Rev. B* **50** 17953

[37] Kresse G and Joubert D 1999 *Phys. Rev. B* **59** 1758

[38] Kresse G and Furthmüller J 1996 *Phys. Rev. B* **54** 11169

[39] Grimme S, Antony J, Ehrlich S and Krieg H 2010 *The Journal of Chemical Physics* **132** 154104

[40] Tonner R, Rosenow P and Jakob P 2016 *Phys. Chem. Chem. Phys.* **18** 6316

[41] Smith D G A, Burns L A, Patkowski K and Sherrill C D 2016 *J. Phys. Chem. Lett.* **7** 2197

[42] Souza P H, Deus D P D A, Brito W H and Miwa R H 2022 *Phys. Rev. B* **106** 155118

[43] Błoński P and Hafner J 2009 *Phys. Rev. B* **79** 224418

[44] Qiao J, Pan Y, Yang F, Wang C, Chai Y and Ji W 2018 *Sci. Bull.* **63** 159

[45] Shi K, Sun Y, Yan J, Deng S, Wang L, Wu H, Hu P, Lu H, Malik M I, Huang Q and Wang C 2016 *Adv. Mater.* **28** 3761

[46] Shen F, Zhou H, Hu F, Wang J, Wu H, Huang Q, Hao J, Yu Z, Gao Y, Lin Y, Wang Y, Zhang C, Yin Z, Wang J, Deng S, Chen J, He L, Liang T, Sun J R, Zhao T and Shen B 2021 *J. Am. Chem. Soc.* **143** 6798

[47] Schrieffer J R and Wolff P A 1966 *Phys. Rev.* **149** 491

[48] Bruno P and Chappert C 1991 *Phys. Rev. Lett.* **67** 1602

[49] Heinrich B and Cochran J F 1993 *Adv. Phys.* **42** 523

[50] Matsukura F, Ohno H, Shen A and Sugawara Y 1998 *Phys. Rev. B* **57** R2037